Geophysical Journal International

Geophys. J. Int. (2012) **190,** 1257–1270 doi: 10.1111/j.1365-246X.2012.05555.x

Seismic wave attenuation from borehole and surface records in the top 2.5 km beneath the city of Basel, Switzerland

Falko Bethmann,[1] Nicholas Deichmann[2] and P. Martin Mai[3]

[1] *Geo-Energie Suisse AG, Reitergasse* 11, 8004 *Zurich, Switzerland. E-mail: f.bethmann@geo-energie.ch*
[2] *Institute of Geophysics, Swiss Seismological Service, ETH Zurich, NO, Sonneggstrasse* 5, 8092 *Zurich, Switzerland*
[3] *Division of Physical Sciences and Engineering,* 4700 *King Abdullah University of Science and Technology, Thuwal* 23955-6900, *Kingdom of Saudi Arabia*

Accepted 2012 May 22. Received 2012 April 29; in original form 2011 July 15

SUMMARY

We investigate attenuation (Q^{-1}) of sediments of 2.5–3.5 km thickness underneath the city of Basel, Switzerland. We use recordings of 195 induced events that were obtained during and after the stimulation of a reservoir for a Deep Heat Mining Project in 2006 and 2007. The data set is ideally suited to estimate Q as all events are confined to a small source volume and were recorded by a dense surface network as well as six borehole sensors at various depths. The deepest borehole sensor is positioned at a depth of 2.7 km inside the crystalline basement at a mean hypocentral distance of 1.8 km. This allows us to measure Q for frequencies between 10 and 130 Hz. We apply two different methods to estimate Q. First, we use a standard spectral ratio technique to obtain Q, and as a second measure we estimate Q in the time domain, by convolving signals recorded by the deepest sensor with a Q operator and then comparing the convolved signals to recordings at the shallower stations. Both methods deliver comparable values for Q. We also observe similar attenuation for P- and S- waves ($Q_P \sim Q_S$). As expected, Q increases with depth, but with values around 30–50, it is low even for the consolidated Permian and Mesozoic sediments between 500 and 2700 m.

Key words: Fourier analysis; Seismic wave attenuation; Wave propagation.

GJI Seismology

1 INTRODUCTION

The city of Basel, Switzerland, was chosen for a geothermal project (hot dry rock technique) to exploit the geothermal potential of the crystalline rock below the sediments of the Rhine Graben. Water was injected under high pressures at 5 km depth to increase rock permeability for subsequent water circulation (Häring *et al.* 2008). Operations were stopped after an induced earthquake of magnitude $M_L = 3.4$ was widely felt within the city of Basel, where macroseismic intensities (Ripperger *et al.* 2009) reached IV–V (EMS-98). Subsequently, ground motion studies were carried out to model the observed intensities and to assess effects of stronger events that might occur in the future.

Previous work in the area used seismic reflection and refraction data to construct a 1-D velocity model (Fäh & Huggenberger 2006), while a 3-D viscoelastic model was derived based on shallow borehole data and from measurements of the fundamental frequency of resonance (Kind 2002). Such models were then used for deterministic earthquake scenarios for the Basel area (Opršal *et al.* 2005; Ripperger *et al.* 2009). Whereas velocity and density information is well defined in those models, attenuation especially of deeper formations remained unknown and some 'best guesses' were made.

Recent work to model the shaking levels induced by the M_L 3.4 earthquake of 2006 showed that modelled ground motions based on the 1-D and 3-D models were in general agreement with the observed macroseismic intensities. However, some peak-ground-velocity observations could not be matched and were attributed to an incorrect representation of attenuation (Q^{-1}) in those models (Ripperger *et al.* 2009).

A further motivation to study Q in the Basel area is the importance of attenuation corrections in source parameter studies. Discussion about the scaling of source parameters has been continuing for more than two decades within the scientific community. An example is the question whether or not the scaled energy of earthquakes increases with magnitude. While many studies see an increase (among others, Kanamori *et al.* 1993; Prejean & Ellsworth 2001; Mayeda *et al.* 2005) other studies find apparent stress to be approximately constant (e.g. Choy & Boatwright 1995; Ide & Beroza 2001; Prieto *et al.* 2004). Some of the differences seen between different data sets can be attributed to non-uniform processing, effects of finite bandwith and variable site-and-path conditions (Ide & Beroza 2001). High-resolution broad-band recordings, uniformly processed and augmented with close by borehole stations, may help to improve such source parameter studies.

In this study, we investigate the attenuation characteristics of the sediments below the city of Basel, using the excellent data due to induced events that were acquired by numerous surface stations and

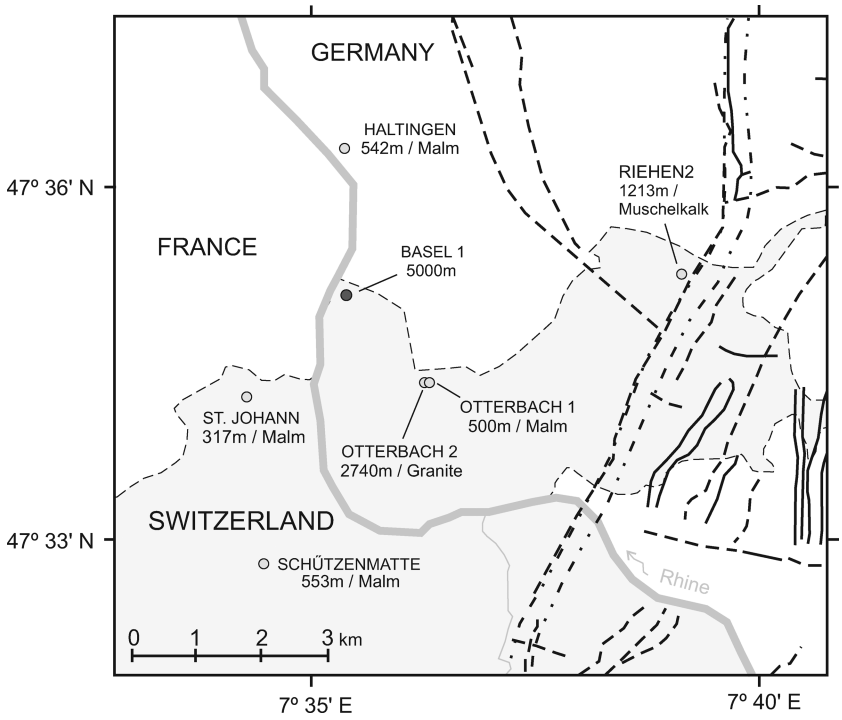

Figure 1. Tectonic map of the southern Upper Rhine Graben after Gürler *et al.* (1987) and Dyer *et al.* (2010). Solid lines show known faults, dashed lines inferred faults and dashed-dotted lines outline the flexure zone and main boundary fault zone. Borehole stations are given with depth and the formation in which sensors are installed. Basel 1 shows the injection borehole.

a six-station borehole array during and after the stimulation phase of the hot-dry rock project.

Previous work on attenuation measurements from borehole recordings is summarized in the paper of Abercrombie (1998). Near-surface attenuation appears to be independent of rock type, and decreases with depth (e.g studies of Hauksson *et al.* 1987; Jongmans & Malin 1995; Abercrombie 1997). Attenuation is found to be very strong in the near surface ($Q \sim 10$ in the upper 100 m) and then becomes less important ($Q \sim 1000$) at depths greater than about 3 km (Abercrombie 1998). Attenuation estimates using the P wave (Q_P) lead to similar values compared to those using the S wave (Q_S) for studies of attenuation in sediments at the Varian well in California (Abercrombie 1998). For attenuation in a granitic environment at Cajon Pass, Abercrombie (1997) finds $Q_S \sim \frac{1}{2} Q_P$ to $Q_s \sim \frac{2}{3} Q_P$. In terms of frequency dependence, attenuation for earthquakes at seismogenic depths is found to decrease from 1 to 10 Hz (Kinoshita 2008) or to be constant (Edwards *et al.* 2011). For frequencies above 10 Hz attenuation is found to be constant (Abercrombie 1995) or slightly decreasing with frequency in the range of 10–100 Hz (Abercrombie 1998).

In this study, we apply two different methods to estimate attenuation. We apply a standard spectral ratio technique to obtain Q independent of frequency and then compare the results to Q determined in the time domain from pulsewidth measurements. Additionally, we estimate Q values between nearby borehole sensors at various depths, and between borehole stations and surface stations across the city of Basel and surroundings.

2 GEOLOGICAL AND TECTONIC SETTING

The city of Basel is located in northwestern Switzerland at the southern end of the Rhine Graben. The fault pattern in the vicinity of Basel (Fig. 1) consists of three sets of faults striking NNE, ENE and NW (Häring *et al.* 2008). These basement fracture zones represent zones of weaknesses in the lithosphere and are sources of seismic activity along the Rhine Graben, where strain is localized and tectonic stress is released.

In 1356, the city of Basel was hit by the strongest historically known earthquake north of the Alps with an estimated moment magnitude around 6.5 (Fäh *et al.* 2009). The regional stress field can be characterized by a strike-slip regime with a substantial normal faulting component. Slip occurs mainly on either NNE–SSW or WNW–ESE striking faults (e.g. Deichmann & Giardini 2009). Horizontal displacement rates are in the order of 0.05 mm per year (Ustaszewski & Schmid 2007) and vertical displacement is in the order of 0.2 mm per year (Rózsa *et al.* 2005).

Beneath the city of Basel, the basement surface consists of weathered granite and is overlain by sediments of about 2.5 km thickness. The sedimentary cover consists of Quaternary, Tertiary, Mesozoic and Permian sediments (Häring *et al.* 2008). Approximately 800 m of sandstone (Buntsandstein and Rotliegendes) are followed by layers of marls and limestone (Fig. 2). The marls contain bands of evaporite that lie between 1.3 and 1.6 km depth (Jordan 1994; Sommaruga 1999; Becker 2000) and constitute horizons of possible stress detachment (Becker *et al.* 1987; Evans & Roth 1998; Valley & Evans 2009).

3 SEISMIC NETWORKS

The seismic data analysed in this article was acquired by three separate institutions. Borehole sensors of Geothermal Explorers Ltd. were placed at six different locations, at depths of 2740 (OTER2), 1213 (RIEH2), 553 (MATTE), 542 (HALTI), 500 (OTER1) and 317 m (JOHAN). The deepest sensor OTER2 is located in the crystalline basement, whereas the other borehole sensors are situated

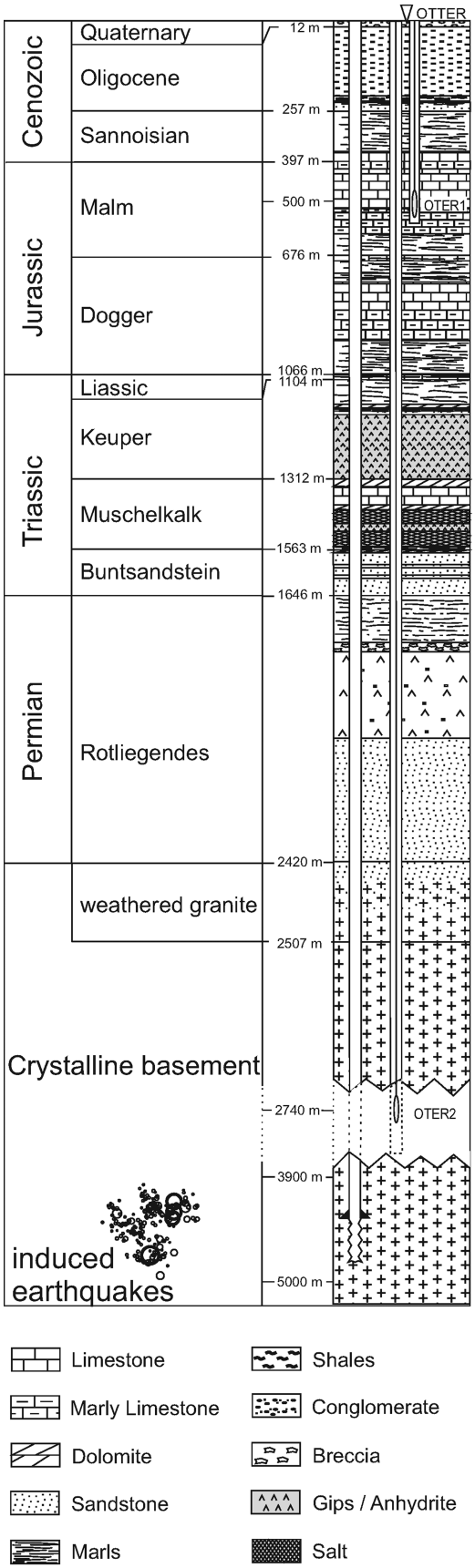

Figure 2. Overview of the borehole profile in the injection well Basel 1. Depths are defined using gamma-ray and caliper logs and are measured from surface (top of drilling basement).

in limestones at different depths (Fig. 1). Surface records are from data of the Landeserdbebendienst Baden Württemberg in Germany (LED), recorded by one high-gain seismometer and six accelerometers and data from the Swiss Seismological Service (SED) recorded by 15 accelerometers. The borehole sensors are short-period geophones with a natural frequency between 4.5 and 5 Hz and a damping coefficient of 0.21. Borehole seismograms are recorded at a sampling rate of 1000 Hz. The signals of the high-gain station of the LED (WL12) are recorded by a 1s seismometer and digitized at a rate of 62.5 Hz. Accelerometer data of the SED is generally sampled at 250 Hz, whereas those of the LED are sampled at 100 Hz. A detailed description of networks and instruments can be found in Deichmann & Giardini (2009) and Baer *et al.* (2007). An overview over the station distribution in the Basel region is given in Fig. 3.

4 DATA AND PROCESSING

The data set for the estimation of attenuation consists of 195 events with M_L ranging between 0.7 and 3.4, with the majority of events (178) of $M_L \leq 2$. Focal mechanisms could be determined for 49 events, six are normal faulting mechanisms and two are strike-slip mechanisms with a strong normal component; all others exhibit strike-slip mechanisms with mostly NS–EW striking nodal planes (Deichmann & Ernst 2009). Hypocentres of the induced events are mainly confined to a NNW–SSE oriented lens-shaped cloud, about 1.2 km in diameter and 200 m wide, at depths between 4 and 5 km (Deichmann & Giardini 2009). A detailed overview of the project can be found in Häring *et al.* (2008). First analyses of the induced microseismicity have been published by Kumano *et al.* (2007), Asanuma *et al.* (2007), Dyer *et al.* (2008) and Deichmann & Giardini (2009).

Waveforms recorded at the deepest borehole sensor OTER2 at 2740 m depth are significantly different compared to recordings at shallower stations. In Fig. 4, we show examples of recordings of three stations situated almost on top of each other. The time delay between *P*- and *S*-phase at station OTER2 is typically about 0.2 s, which limits the time window for waveform analysis. The event shown is one of the strongest recorded events, and the P_g and S_g waves are well captured within the shown time window (indicated by the black bar in Fig. 4). Time windows generally start 0.04 s prior to the selected phase arrival and end before the reflected phase reaches the sensor. This is to avoid distortion of upcoming phases by surface reflections, making the spectra of the downhole seismogram anomalously deficient in certain frequencies (Shearer & Orcutt 1987). For example, at station OTER1 at 500 m depth, we use a window length of 0.35 s for the P_g wave and 0.5 s for the S_g wave. For surface stations, we generally choose a time window of 0.5 s for analysis. We also repeat all calculations with a constant 0.2 s time window to examine the dependence of Q on the choice of window length. We find the variations of Q due to window length to be around ± 7 per cent for surface stations and less for borehole sensors. To measure noise, we pick a time window of similar length to the one used for spectral analysis. It starts prior to the onset of the picked phase. For S_g waves of the deepest borehole sensors the noise interval thus contains parts of the *P*-wave coda.

The ray paths between the source region and selected borehole and surface sensors, calculated with a 2-D ray tracing algorithm (Gebrande 1976), are shown in Fig. 5. Three different velocity models, selected after Ripperger *et al.* (2009), are chosen to represent the progression of the Rhine Graben underneath the city of Basel. Moving away from the injection borehole (model 1), the thickness of

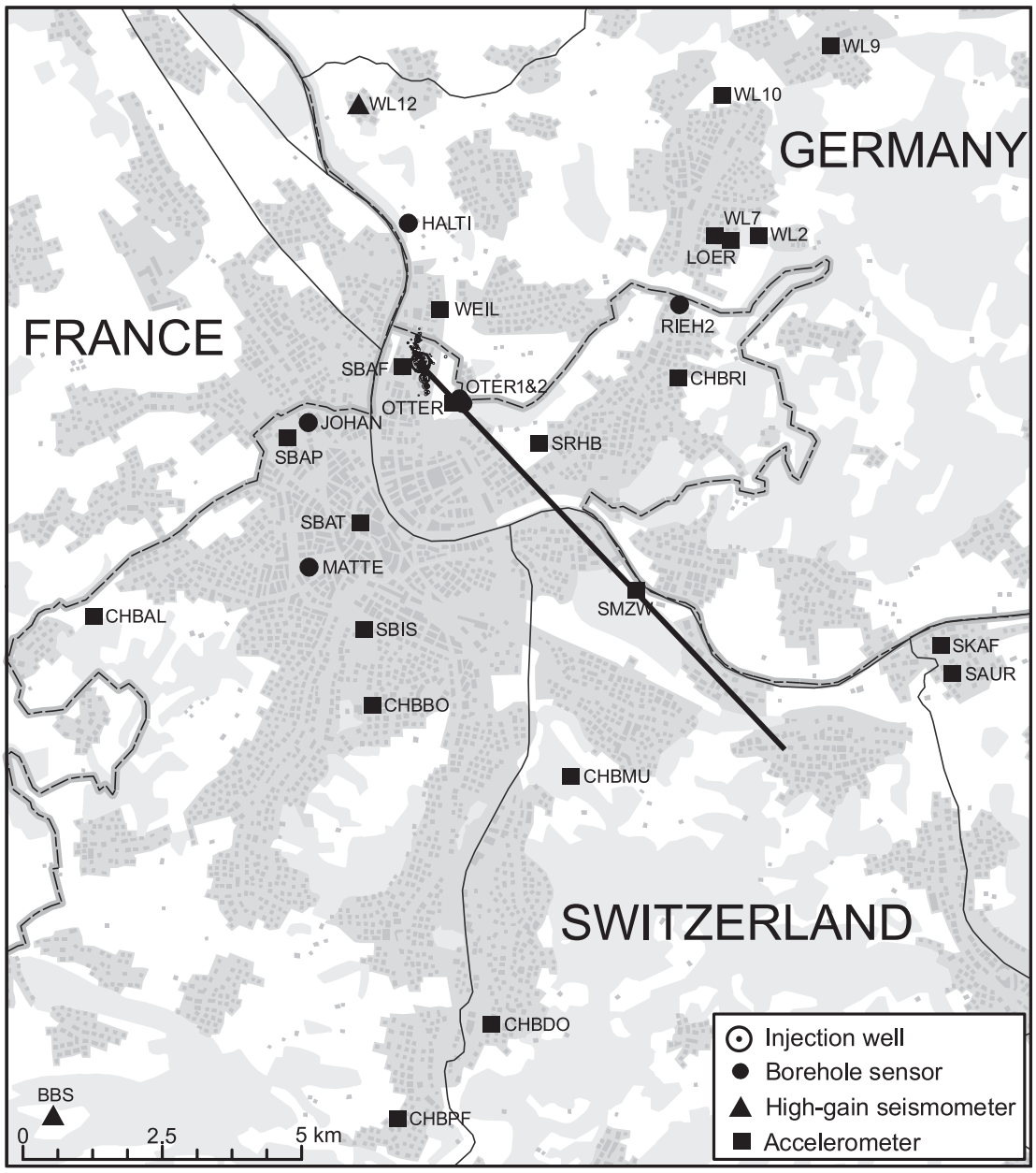

Figure 3. Station network in the city of Basel and surroundings during the time period of 2006 December to mid 2007. Shown are stations that were used for *Q*-analysis. The epicentres of the induced events are shown as small circles between stations SBAF and OTER1. The black line indicates the profile used for ray tracing in Fig. 5.

sediments increases while the seismic velocities decrease (model 2). At a radial distance of about 6 km from the borehole the edge of the Rhine Graben is reached, where the basement is covered by approximately 250 m of Triassic sediments (model 3). We observe that the rays reach the sensors at almost vertical incidence (5°–16° depending on distance). Thus, the calculated amplification factor for *P* waves is approximately 1.95. For *S* waves, we assume a free surface amplification factor of 2 (S_H phase, Aki & Richards 2002).

As the orientation of borehole sensors is not known, we rotate all seismic recordings into the direction of maximum energy using the method of Jackson *et al.* (1991). It provides estimates of signal and noise energy and the degree of rectilinearly of polarization (Esmersoy 1984). In the case of borehole stations and for the *P* wave, we use all three velocity components for rotation, in case of the *S* wave, where the wave encounters the surface sensor at an almost vertical angle, we rotate the horizontal components only (S_H phase).

After rotation, we interpolate all recordings to 1000 Hz by adding zeroes to the Fourier transform (FT) and then calculating the inverse FT. This is done to have a uniform frequency axis for all spectral ratios and to increase the number of points in the time domain for subsequent tapering. However, it does not alter the original frequency content of the signals. Following Thomson (1982), we then apply a multitaper to optimize the resistance to spectral leakage. The multitaper method has been widely used in geophysical applications and performs better than standard individual taper methods (Park *et al.* 1987; Bronez 1992; Riedel & Sidorenko 1993). However, it does lead to a bias at lower frequencies (Prieto *et al.* 2007). Examples of displacement spectra for stations OTER2, OTER1 and OTTER for the magnitude 2.2 event in Fig. 4 are shown in Fig. 6.

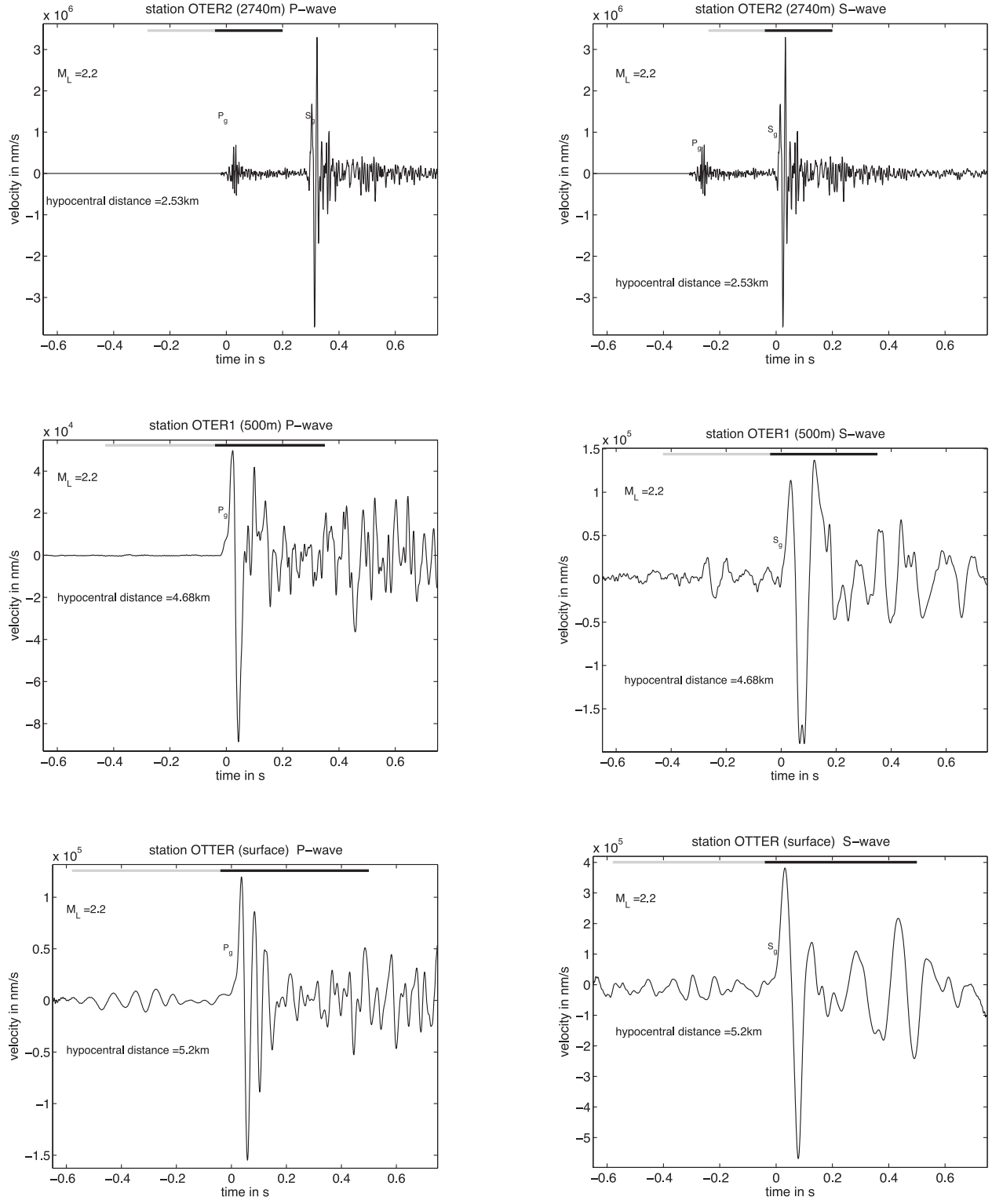

Figure 4. Comparison of velocity seismograms recorded at stations OTER2, OTER1 and OTTER situated on top of each other. Shown is the seismogram of a magnitude M_L 2.2 event rotated into the direction of maximum energy. The grey bar indicates the interval taken for noise and the black bar the interval taken for waveform spectral analysis. Notice the decrease of high frequency content at station OTER1 compared to station OTER2 - an indication of high attenuation also at greater depth.

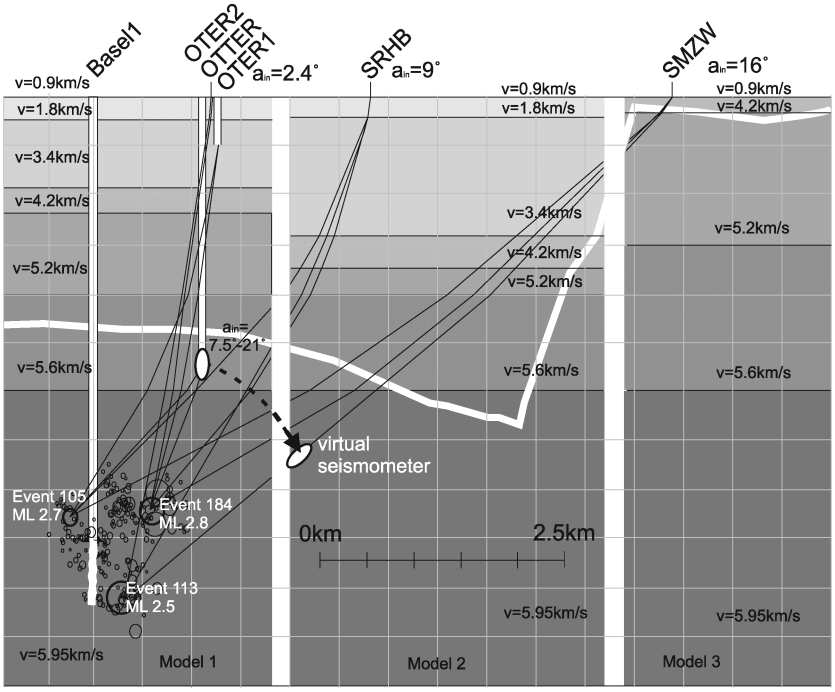

Figure 5. Cross section in NW–SE direction along the black line in Fig. 3. Shown are results of the 2-D ray tracer (Gebrande 1976). Velocity profiles are taken from Ripperger *et al.* (2009). The white line shows the top of the crystalline basement. Rays encounter the surface at almost vertical incidence (denoted by angle a_{in}).

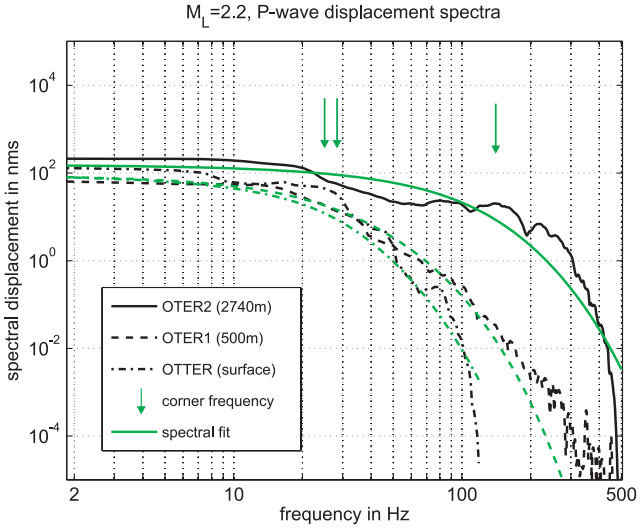

Figure 6. Displacement spectra for the magnitude 2.2 event shown in Fig. 4. Note the decrease of high frequency content towards the surface. Corner frequency estimates (green arrows) for surface or shallow borehole data need to be corrected for attenuation to obtain correct values (Singh & Ordaz 1994; Prejean & Ellsworth 2001).

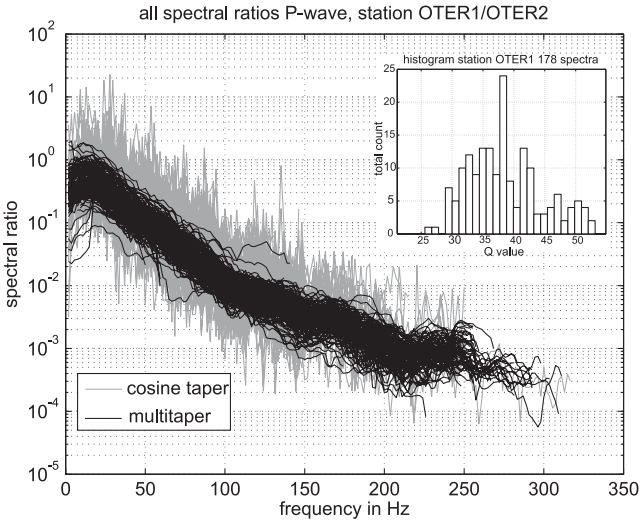

Figure 7. Spectral ratios for 178 events recorded at station OTER2 and OTER1. Spectral ratios shown in grey were obtained using a cosine shaped taper applied over 5 per cent of the waveform, the black ratios show the results using a multitaper approach. Plotted are intervals for which signal-to-noise ratios exceed a value of 5. The histogram in the top right corner shows the distribution of Q values determined from each single spectral ratio.

In Fig. 7, we demonstrate the advantage of a multitaper over a cosine shaped taper and show the spectral ratios estimated at station OTER1 over the complete frequency range (1–320 Hz).

5 METHODS FOR ESTIMATING Q

We apply two different methods to estimate attenuation. First, we use a standard spectral ratio technique to obtain Q independent of frequency. As a second measure, we estimate Q in the time domain by convolving signals recorded at the deepest station with a Q operator and comparing the convolved signal to recordings of a shallower station.

5.1 Spectral ratios

Under the assumption of a frequency independent Q, the ratio between the spectrum of an event recorded by a shallow station and the spectrum of the same event recorded at a deeper station will

follow an exponential decay (Abercrombie 1997)

$$A(f) = A_0 e^{-\pi f \frac{\Delta t}{Q}}, \tag{1}$$

where $A(f)$ is the amplitude ratio, A_0 is the amplification at 0 Hz and Δt the traveltime between two stations. The average Q between the two stations is then calculated by

$$Q = -\frac{\pi \Delta t}{m}, \tag{2}$$

with proportionality factor m determined by a linear regression of the spectral decay in a log-linear plot. The spectral ratio method is well established and has been applied in numerous studies (e.g. Hauksson *et al.* 1987; Aster & Shearer 1991; Prejean & Ellsworth 2001).

In this study, we calculate spectral ratios for all recorded earthquakes between a deep and a shallow station, and then obtain the final spectral ratio by computing the mean of all ratios at a particular frequency. Taking the median instead of the mean spectral ratios provides similar results. Only frequencies are considered with signal-to-noise ratios greater than 5 for the *P* wave and greater than 2 for the *S* wave. This is a subjective choice, as calculations with signal-to-noise ratios between 2 and 10 lead to changes in the spectral ratios at high and low frequencies (for which the signal-to-noise ratio is generally lower), but leave the central part of the spectrum unchanged. Q is then calculated via eq. (2) by a weighted fit. The weighting is based on the number of computed spectral ratios and the standard deviation at each frequency. Furthermore, we only consider frequency bins that contain 10 or more measurements. In so doing, we focus on the most reliable part of the spectrum, where we have the most recordings and get less bias from high and low frequencies, where we generally have fewer recordings and a lower signal-to-noise ratio. Furthermore, we only consider frequencies above 10 Hz for the regression. This is done to remove resonance effects at the natural frequency of the underdamped borehole sensors (although corrected for) at around 5 Hz and to avoid the potential bias due to multi-taper effects Prieto *et al.* (2007) and due to the potential transition of Q to lower values (Abercrombie 1998). An example of a linear fit to 178 spectral ratios between station OTER2 and OTER1 is shown in Fig. 8.

Due to the stacking and the generally large number of spectra, fitting the smooth mean spectrum leads to mathematically small uncertainties (small confidence intervals, see Table 1). However, these purely mathematical confidence intervals do not account for other, more physical sources of uncertainty, like the selection of the spectral window for the regression. Potential additional uncertainties related to (secondary) effects are not considered either, such as resonance effects (site amplification) between different layers where significant impedance contrasts exist. To examine uncertainties of Q due to parameter choices in the data processing, we repeated all calculations, (a) varying the signal-to-noise ratio threshold (2 and 5 resulting in a ΔQ of ∼2 per cent), (b) processing window length (from 0.2 to 0.5 s, where applicable, resulting in a ΔQ of ∼6 per cent), (c) changing the number of prolate spheroidal sequences for the multitaper (2–8 resulting in a ΔQ of ∼4 per cent) and (e) the range of frequencies for the regression (10–45; 35–70 and 60–95 Hz where applicable, resulting in a ΔQ of ∼11 per cent). The resulting total variation in Q is expressed in Table 1 as a range of Q values obtained by choosing different processing parameters. To further examine the variability in Q for a given station pair, we compute Q for single spectral ratios of the corresponding events. The histogram inset in Fig. 7 shows the variability of Q estimated for the station pair of OTER2 and OTER1 from these single spectral ratios; the result is a mean Q of 38 and a standard deviation of 8.

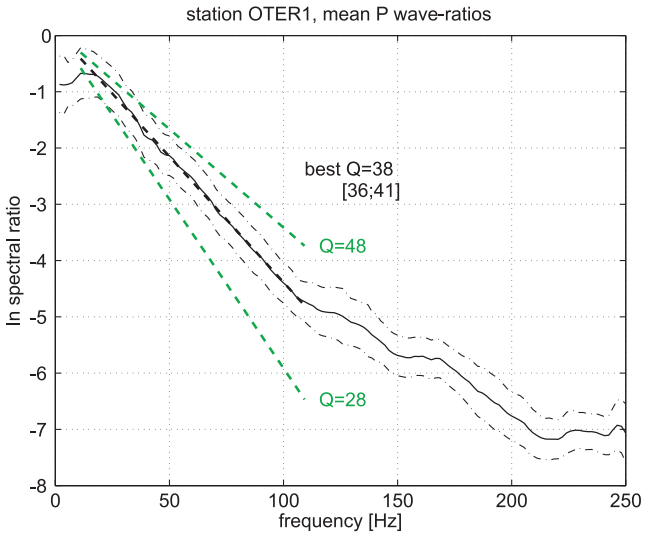

Figure 8. Mean spectral ratios between station OTER2 and OTER1. The black dashed line indicates the frequency range of a linear fit to determine Q. The thin dashed lines show one standard deviation, the green lines indicate how a fit would look like for different Q values. A transition to higher Q values can be observed above 100 Hz which is also seen for other borehole stations. The number in brackets show the range of Q values for varying processing parameters (signal-to-noise, processing window length, number of multitapers and frequency range of spectral fit).

5.1.1 The influence of differences in take-off angle

The deepest borehole sensor is positioned inside the crystalline basement at a mean hypocentral distance of 1.8 km. Under the assumption that attenuation does not vary within the crystalline basement, we want to estimate attenuation between this deep station and all shallower stations. These stations are distributed across the city of Basel and around the borehole. To correct for differences in radiation pattern and take-off angle, we assume a 'virtual' borehole station OTER2 that is positioned in the propagation direction to the shallower stations (Fig. 5) and estimate correction factors obtained by a theoretical analysis as described later.

The position of the seismometer with respect to the earthquake fault affects the recorded waveform and consequently also the spectral ratios. A difference in radiation coefficient results in a constant upward or downward shift of the spectral ratio in a log ratio versus frequency plot, but leaves the spectral decay unchanged. However, viewing the source under different take-off angles will affect the shape of the apparent source-time function, thus leading to different corner frequencies and changes in the spectral content.

To estimate the error in Q caused by calculating spectral ratios for different take-off angles, we start with a theoretical source time function from a circular source with variable rupture velocity (Sato 1994; Deichmann 1997). Attenuation along the propagation path is represented by a convolution of the far field displacement pulse with causal Q operators (Azimi *et al.* 1968). Spectral ratios are then calculated between spectra for different take-off angles at various depths and distances.

Input parameters to compute the source time function are moment (M_0), phase velocity at the source (c), stress drop ($\Delta\sigma$), average rupture velocity ($\overline{v_r}$), the rates of the duration of rupture acceleration

Table 1. Q values obtained by spectral ratios. Stations with depth specification are borehole sensors, station names starting with S are strong motion stations as well as station OTTER, stations starting with CH are part of a temporary strong-motion network. Station names starting with W and station LOER are stations of the German network. The correction factor denotes the correction of Q needed to compensate for the difference in take-off angles. $\overline{Q}$ values are obtained by a quantitative comparison of shallow and deep Q to an averaged Q along the travel path (see Section 6 for details). Errors of Q_P and Q_S in columns 3 and 6 are obtained from the weighted fit to the stacked spectra, columns 4 and 7 show the variability of Q when processing parameters (window length, frequency range, signal-to-noise threshold, multitaper windows etc.) are changed.

Q estimated from	to station	Q_P	range Q_P	Number of spectra used	Q_S	range Q_S	Number of spectra used	Q_P time-domain	Mean take-off angle θ	Frequency range of fit (P|S)		Mean hypo-central dist.	$\Delta\theta$ corr. factor P|S		$\overline{Q}$
	RIEH2 (1213 m)	84 ± 3	[83–90]	180	86 ± 4	[81–102]	119	72 ± 13	68°	11–98Hz	11–52 Hz	6.0 km	1	1	
	MATTE (553 m)	54 ± 1	[39–57]	188	63 ± 2	[59–92]	95	53 ± 16	46°	11–130 Hz	11–39 Hz	5.9 km	1.17	1.12	
	HALTI (542 m)	49 ± 1	[38–54]	188	58 ± 5	[58–76]	50	50 ± 14	67°	11–130 Hz	11–30 Hz	4.7km	1	1	
	OTER1 (500 m)	38 ± 1	[37–41]	178	–			42 ± 12	71°	11–109Hz	–	4.3 km	1		
	JOHAN (317 m)	48 ± 1	[48–58]	185	40 ± 2	[40–98]	54	58 ± 13	65°	11–98Hz	11–30 Hz	4.8 km	1	1	
	CHBAL	53 ± 1	[52–57]	29	–				48°	11–76 Hz	–	8.8 km	1.02		
	CHBBO	37 ± 1	[33–39]	33	–				34°	11–81Hz	–	7.9 km	1.04		
	CHBDO	42 ± 2	[38–64]	15	–				22°	26–43 Hz	–	13.0 km	1.06		
	CHBMU	29 ± 1	[28–30]	32	–				40°	11–48Hz	–	9.4 km	1.05		
	CHBRI	41 ± 1	[41–44]	32	–				73°	11–89 Hz	–	6.7 km	1.04		
	LOER	26 ± 1	[22–46]	19	–				65°	11–33Hz	–	7.0 km	1		
	OTTER	32 ± 1	[28–33]	104	39 ± 1	[35–64]	88	45 ± 7	72°	11–83 Hz	11–35 Hz	4.8 km	1	0.99	33
OTER2 (2740 m)	SAUR	105 ± 4	[87–114]	59	96 ± 4	[83–120]	38		55°	11–69 Hz	11–33 Hz	12.2 km	1.03	1.03	
mean $\theta = 68°$	SBAF	31 ± 1	[25–31]	126	39 ± 2	[33–68]	45		79°	11–120 Hz	11–31 Hz	4.6 km	1	0.98	29
	SBAP	37 ± 2	[36–46]	122	40 ± 2	[39–65]	35		63°	11–69 Hz	11–30 Hz	5.3 km	1.01	1.01	31
	SBAT	31 ± 1	[29–34]	128	44 ± 7	[33–73]	11		52°	11–89 Hz	24–30 Hz	5.6 km	0.99	1.04	
	SBIS	42 ± 1	[41–47]	141	52 ± 2	[52–82]	13		42°	11–89 Hz	11–30 Hz	6.9 km	0.98	1.06	36
	SKAF	128 ± 4	[95–135]	87	123 ± 2	[98–154]	63		58°	11–98Hz	11–41 Hz	11.8 km	0.99	1.04	
	SRHB	35 ± 1	[35–37]	73	41 ± 2	[41–76]	13		64°	11–83 Hz	11–30 Hz	5.4 km	1	1.01	34
	SMZW	46 ± 1	[38–50]	62	–				50°	11–89Hz	–	7.5 km	0.99		
	WL2	27 ± 1	[27–36]	22	–				61°	11–39Hz	–	8.1 km	1.01		
	WL7	29 ± 1	[28–38]	19	–				63°	11–39Hz	–	7.7 km	1.01		
	WL9	46 ± 4	[46–70]	16	–				55°	11–33Hz	–	10.4 km	1.02		
	WL10	34 ± 1	[34–43]	14	–				55°	13–39Hz	–	8.6 km	1.02		
	WL12	73 ± 12	[73–104]	20	–				55°	11–24Hz	–	6.5 km	1.03		
	WEIL	31 ± 3	[28–51]	21	–				83°	11–48Hz	–	4.7 km	0.96		
	CHBRI	12 ± 1	[12–16]	28	–				73°	26–89Hz	–	6.7 km	1		
RIEH2 (1213 m)	LOER	6 ± 1	[5–11]	21	–				65°	26–39Hz	–	7.0 km	1.01		
mean $\theta = 68°$	WL7	11 ± 1	[10–16]	21	–				63°	20–39Hz	–	7.7 km	0.99		
	WL2	10 ± 1	[9–28]	24	–				61°	20–39Hz	–	8.1 km	1.02		
MATTE (553 m)	SBIS	16 ± 1	[16–20]	125	–				42°	31–80 Hz	–	6.9 km	1.02		
mean $\theta = 46°$															
OTER1 (500 m)	OTTER	24 ± 1	[22–24]	98	–				72°	11–78Hz	–	4.8 km	1		
	SBAF	22 ± 3	[20–23]	11	–				79°	11–89Hz	–	4.6 km	1.01		
mean $\theta = 71°$	SRHB	29 ± 2	[28–32]	68	–				64°	11–40 Hz	–	5.4 km	1		
JOHAN (317 m)	SBAP	18 ± 1	[15–21]	123	23 ± 7	[22–44]	33		63°	11–83Hz	11–19Hz	5.3 km	1	1.01	
mean $\theta = 65°$															

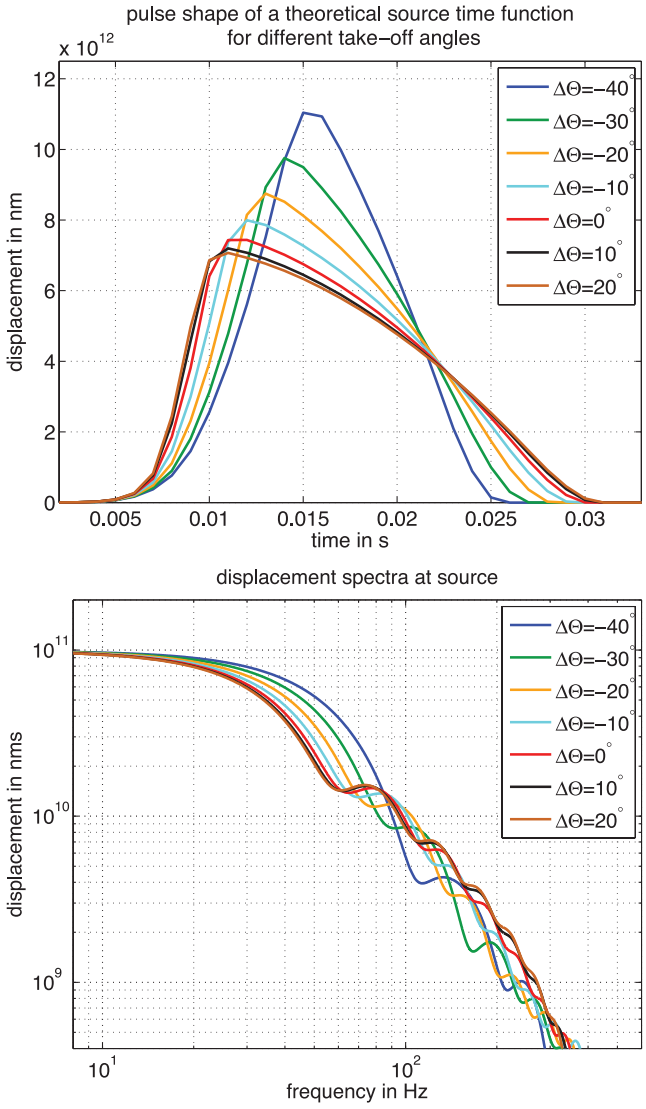

Figure 9. Influences of differences in take-off angle on pulse width and spectral shape. The top figure shows the different shape of a source time function for varying take-off angle. We chose $\theta = 68^\circ$ as reference (take-off angle for rays to station OTER2). The bottom figure shows the corresponding changes in spectral shape. Note the shift of the characteristic lobes in the spectrum to higher frequencies for smaller take-off angles.

and deceleration relative to the total rupture time(k_1,k_2), steepness of velocity increase (q) and angle between ray and fault normal (θ) (see Deichmann 1997, for details).

We choose parameters that represent a typical induced event of $M_w = 1.3$: c is given by borehole logs ($c = 5940\,\mathrm{m\,s^{-1}}$), $q = 1$, $k_1 = 40$ per cent and $k_2 = 10$ per cent are chosen to obtain an emergent onset of the modelled P wave. Source parameter $\Delta\sigma$ is set to 0.3 MPa and $\overline{v_r}$ to 2500 $\mathrm{m\,s^{-1}}$ which corresponds to 75 per cent of the velocity of the S wave. Pulse and spectral shapes for different values of θ are shown in Fig. 9.

In Fig. 10, we show how the spectral shape changes with distance and take-off angle (top figures). Lobes in the spectra become smoother with increasing distance and higher attenuation. However, at station OTER2 such lobes are still significant and may lead to wrong Q estimates. The bottom left figure shows how the characteristic lobe observed at 60 Hz for OTER2 results in deviations of the spectral ratios from a straight line. With an increasing difference in take-off angle, a higher deviation is observed. The bottom right figure depicts the error of Q for an improper regression between 10 and 50 Hz.

Using a theoretical source time function as described above and calculating spectral ratios between the deepest station OTER2 and a borehole sensor at 2.2 km distance, step-like changes in slope of the spectral ratios are observed at 60 Hz (Figs 9b and 10a). For the Basel data set, we compute spectral ratios for events of various magnitudes and waveforms of different pulsewidth. Therefore, the observed plateaus in the spectra are smoothed, and occur at different frequencies (Example Fig. 8 at 110, 150 and 210 Hz). When those features can be clearly identified in the spectral ratios, errors in Q can be avoided by restricting the regression to frequencies lower than the observed deviation from a straight line. However, for some stations, and generally for all estimates based on S waves, the frequency range for the regressions is limited due to signal-to-noise constraints. As a consequence such features may not be identified and lead to an erroneous Q estimate. We therefore estimate Q-variability due to a possible error introduced by an unidentified spectral artefact (Table 1). In all cases except one, our estimated errors in Q are less than 6 per cent. The small errors result from a combination of high attenuation ($Q < 50$) over distances greater than 5 km and generally small differences in take-off angle. However, in case of lower attenuation, a smaller station to station distance and/or a greater difference in take-off angle, such errors may become significant (e.g. station MATTE in Table 1).

5.2 Time-domain Q estimation

To obtain an independent measure, we also estimate Q in the time domain. We take the waveform recorded at a deeper borehole sensor and convolve it with a causal Q operator (Azimi *et al.* 1968). The convolved signal is compared to signals recorded at shallower stations, and Q is then obtained by minimizing the misfit between the real and convolved signal in a forward-modelling approach.

For the estimation of Q, we manually select simple waveforms (similar to the ones shown in Fig. 11) from a subset of 49 events for which focal mechanisms are available. The waveforms of the station pairs are corrected for instrument response and normalized to correct for amplification caused by impedance contrast, radiation pattern difference and free surface (if applicable). The waveform of the deeper station is convolved with a suite of Q operators ($Q =$ 1:1:500) and cross-correlated to a recording of the shallower station of 0.3 s length (Fig. 11). We then calculate the misfit between convolved and recorded waveform. To obtain a general Q between station pairs, we calculate the mean over all Q's for the individual events. As documented in Table 1, the mean Q values are in good agreement to those obtained by spectral ratios.

6 RESULTS AND DISCUSSION

We determine attenuation between borehole and shallower sensors using both P_g and S_g waves. For borehole stations positioned in sediments, we select shallower stations in the near vicinity and similar azimuth to estimate Q. For the deepest borehole station OTER2 at 2740 m in the crystalline basement, we extend the spectral ratio method to obtain Q for all shallower stations regardless of azimuth and take-off angle. The results are summarized in Table 1. We find Q values in the range of 30–40 for stations located in the Rhinegraben sediments, and Q increasing with depth to values of

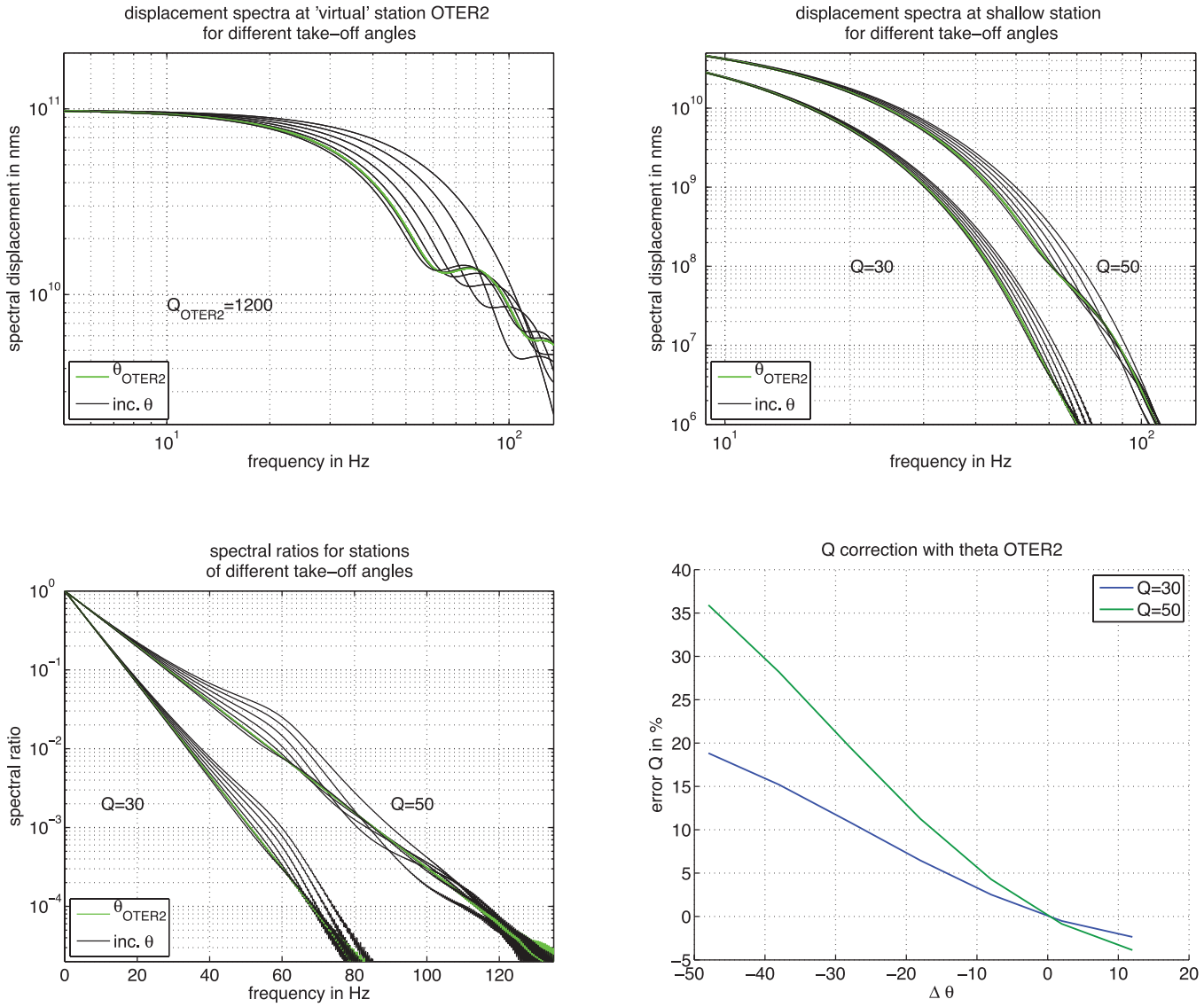

Figure 10. Change of spectral shape with distance and the effect of lobes in the spectra on spectral ratios. The left top figure shows theoretical far field displacement spectra for a magnitude M_w 1.3 earthquake at 1.8 km hypocentral distance. The top right figure illustrates the change in spectral shape for different values of attenuation for a hypocentral distance of 6 km. Characteristic lobes in the spectrum are smoothed with distance and decreasing Q. However, such lobes lead to a deviation from a straight line for spectral ratios of different take-off angle and eventually lead to incorrect Q estimates (left bottom figure). The bottom right figure shows the error in Q when attenuation is obtained by an erroneous regression from 10 to 50 Hz. The error in Q increases with the difference in take-off angle.

~85 at depths between 1 and 2.5 km. Values for Q estimated in the time and frequency domain agree with each other. The errors of Q are low (<5 per cent) due to the many recordings (up to 188) for spectral ratios but are higher (<30 per cent) for time-domain estimates (because a maximum of only 26 events could be used for that analysis). To provide a better indication about the quality of the spectra and the corresponding Q estimate, we also list the frequency range that was used for the regression (Table 1). A wide frequency range is a sign of good signal-to-noise ratios and a reliable regression through many data points, whereas a narrow frequency range is an indication of lower signal-to-noise ratios, less bandwidth and less data points available for the regression. We further show the variation of Q due to the selection of processing parameters.

For most stations, spectral ratios can be approximated by a straight line, suggesting a Q independent of frequency. However, for borehole stations for which the frequency range extends to higher frequencies, a change in slope can be observed at frequencies above 100 Hz (Figs 7 and 8). The deviation is most likely caused by computing spectral ratios from signals recorded at different take-off angles (Section 5.1.1). According to the manufacturer of the borehole instruments, deviations could also be caused by parasitic resonances of the coils within the sensors. Additional uncertainties in Q may arise from unidentified spectral artefacts that occur when spectral ratios are calculated for travel paths with different take-off angles (Section 5.1.1). The error in Q caused by such artefacts is generally lower than 6 per cent and depends on station to station distance, the difference in take-off angle and event magnitude (frequency content). The resulting errors for a typical M_w 1.3 event are listed in Table 1. Note that this error is not accounted for in the determination of Q, as we assume that we are able to identify such artefacts and have limited the frequency range for the spectral ratio regressions so as to avoid their influence.

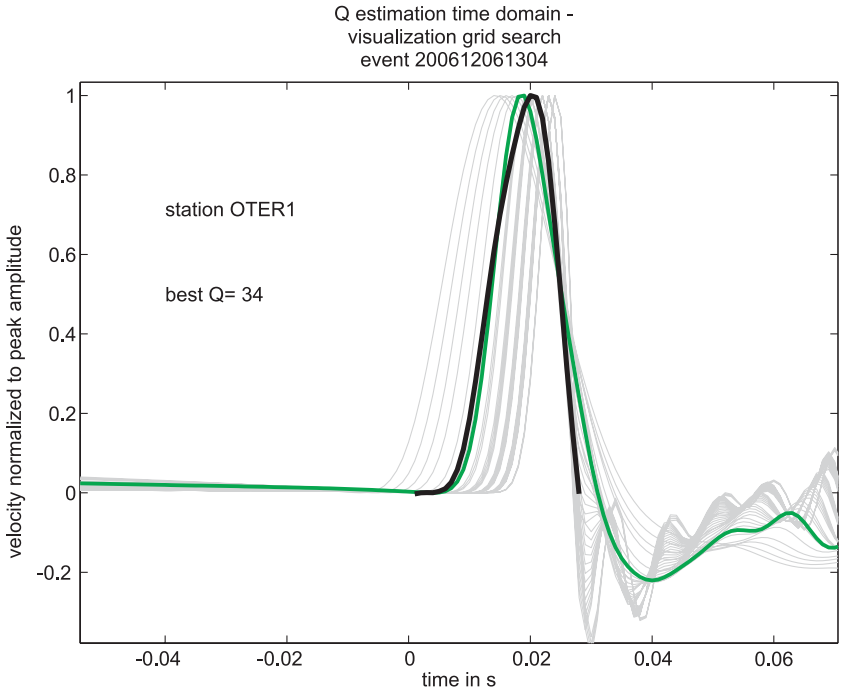

Figure 11. Visualization of our grid search to estimate Q in the time domain. The black waveform shows the recording at station OTER1, the grey curves are recordings from station OTER2 convolved with a causal Q operator. The green curve shows the best fitting pulse.

The assumption of a homogenous subsurface being represented by an equivalent average Q can be a source of error. For example, significant impedance contrast and resonance effects between layers may add to the complexity and lengths of waveforms, and may not be captured in the rather narrow processing window. However, due to the short traveltimes and the attenuation along the ray path such effects result in pulse broadening of the first onset (Fig. 4), and are accounted for when spectral ratios are calculated.

To test the reliability of our results, we further examine the Q estimates in a quantitative and qualitative manner.

Fig. 12 shows the Q values computed for each station on a map with the top of the Triassic sediments in the Basel region. Q measured between borehole stations (red) is compared to Q values estimated between the deepest borehole and surface (black). Plotted in light blue are Q values between shallow boreholes and the surface. A first order observation is that Q increases with depth (light blue > black > red)—the deeper the station, the higher the corresponding Q value. Seismic waves propagating from the deepest station OTER2 to the south/southeast travel through an additional 500 m of Triassic sediments, compared to stations positioned to the north or southwest (e.g. station SRHB in Fig. 5). This accounts for roughly 30 per cent of the ray path. Compared to other stations, this ray path length is high and one may expect higher attenuation at those stations due to sediment depth. However, we do not observe a correlation of Q with Cenozoic and Jurassic sediment depth.

As a further consistency check, we compare Q values estimated between the deepest borehole and the surface to the sum of Q estimates between the deepest to a shallow borehole and from the shallow borehole to the surface. We use the following formula for the comparison, where tt denotes the traveltime

$$\frac{1}{\overline{Q}} = \frac{tt_1}{tt}\frac{1}{Q_1} + \frac{tt_2}{tt}\frac{1}{Q_2}, \tag{3}$$

$\overline{Q}$ and tt are measured between the deepest sensor and the surface, Q_1 and tt_1 from the deepest to the shallower borehole and Q_2 and tt_2 from the shallow borehole to the surface. The results for $\overline{Q}$ are listed in Table 1. $\overline{Q}$ is in good agreement ($\Delta Q = \pm 2$ or 6 per cent) for station pairs of OTER2 (2740 m), OTER1 (500 m) and surface stations in the vicinity of OTER1 (OTTER, SBAF, SRHB), for borehole stations at greater distances (MATTE: 553 m, JOHAN: 317 m) Q differs by $\Delta Q = \pm 6$ or $\sim$16 per cent (OTER2–MATTE–SBIS, OTER2–JOHAN–SBAP) . For station pairs involving borehole sensor RIEH2 (1213 m), we observe a ΔQ of 11–16 (up to 50 per cent). However, this sensor is close to the Rhinegraben flexural zone, and Q estimates for shallower stations involve ray paths through the fault zone. Therefore, $\overline{Q}$ estimates involving borehole station RIEH2 may be questionable.

Finally, Fig. 13 compares attenuation of the sediments in Basel to findings of two studies in California (Jongmans & Malin 1995; Abercrombie 1998). All three studies estimate attenuation in a similar frequency range using borehole data, but for different rock types. The lithology of the Varian well unit consists mainly of sand-, silt- and claystone, compared to sandstone and granite at the Cajon Pass drillhole and to the complex geology below Basel (Fig. 2). Despite the differences in geology, attenuation is similar for all three regions, and also decreases with depth in a similar fashion. Also, we observe no difference in attenuation for rays travelling through thicker sediments (Figs 5 and 12). This confirms previous findings of Abercrombie (1998), that attenuation is more a function of increasing fracture width toward the surface than of rock type. Q is low within the first 300 m ($10 < Q_P \sim Q_S < 30$), and increases to values of $\sim$85 for depths of 2–3 km. Whereas attenuation for S waves is weaker in the study of Abercrombie (1997), similar values of Q_P and Q_S are observed for the Varian well and Basel data. A possible reason could be differences in attenuation mechanism (the fraction of intrinsic to scattering attenuation). A quantitative measurement of the relative contribution of both attenuating mechanisms was introduced by Wu (1985) or Hoshiba (1993), but this approach is not applicable to the Basel data set due to the short seismogram length of the available data segments (<2s). A

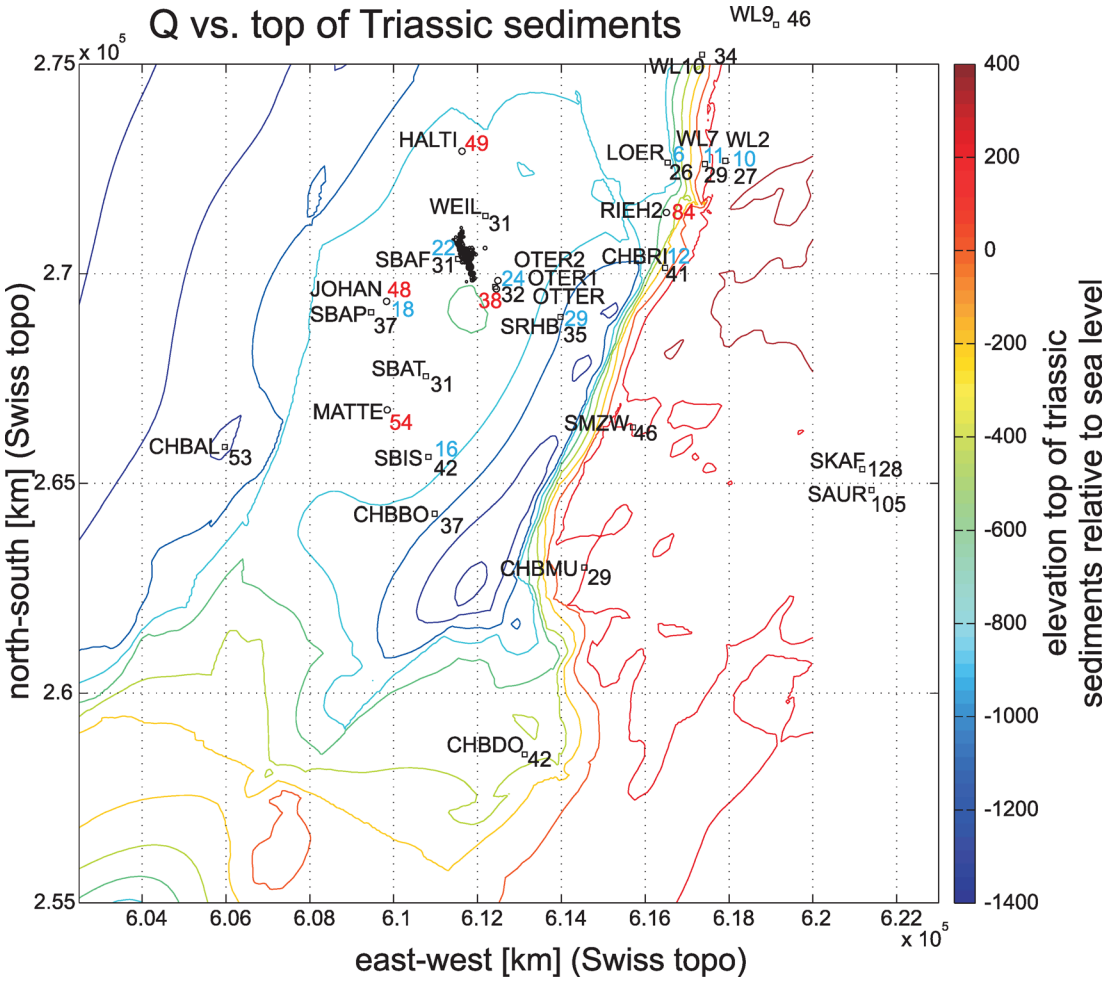

Figure 12. Attenuation versus sediment depth. Red numbers denote Q values measured between the deepest and shallower borehole stations, black numbers to surface stations. Light blue colours represent Q values estimated between a shallow borehole and surface stations in the near vicinity. 3-D geology model after Spottke *et al.* (2005), modified with recent borehole data.

separation between intrinsic and scattering attenuation therefore was not possible. However, findings of Feustel *et al.* (1996) and Jin *et al.* (1994) suggest that intrinsic attenuation is the dominant attenuation mechanism at frequencies used in this study.

As a consequence of rather strong attenuation also at greater depth (>500 m) high frequencies are removed from the seismic recordings (Fig. 4). Waveforms recorded at station OTER2 (2740 m) suggest a pulsewidth of ∼0.01 s compared to a pulse width of ∼0.1 s for recordings at station OTER1 (500 m) for a typical earthquake in this study. Consequently, a simple fit of the spectral content leads to erroneous estimates of the corner frequency ($f_c \sim 1$/pulsewidth) from data recorded at OTER1 alone. This is also shown in Fig. 6. Therefore, great care is required when f_c is used for source parameter studies. Borehole data improve the signal to noise content significantly, with the caveat however, that even shallow boreholes (≤500 m) record only a rather small fraction of the high-frequency radiated by the source.

7 CONCLUSIONS AND OUTLOOK

Using high-quality recordings of induced earthquakes in the city of Basel, Switzerland, we study the attenuation properties in the area. Attenuation (Q^{-1}) of waves emitted from induced earthquakes in the frequency range of 10–130 Hz is strong within the first 300 m ($10 < Q_P \sim Q_S < 30$) and decreases with depth ($Q \sim 85$ at depths of 2–3 km). We obtain similar values of Q for estimates of attenuation in the time and frequency domain. We also observe that $Q_p \sim Q_S$, similar to Jongmans & Malin (1995). Attenuation within the compacted sediments of Basel is independent of rocktype, as no correlation of Q with Cenozoic and Jurassic sediment depth is found. Our results are confirmed when comparing our Q values to the studies of Jongmans & Malin (1995) and Abercrombie (1998), that also infer similar Q values in geologically different environments. Our empirical estimates of attenuation include qualitative and quantitative comparisons; we find that for all stations Q increases with depth and separate Q values along the path add up to a general Q along the entire path. Our Q values are important to constrain attenuation models in the Basel region, needed to conduct realistic seismic wave propagation simulations and for detailed source parameter studies (in which attenuation is critical to correctly infer corner frequency and stress drop). Considering the increasing number of fluid injections into deep formations in the oil and geothermal industry and the associated induced seismicity, realistic estimates of attenuation (including its variability) are necessary to estimate the small-magnitude detection capability of the observational network, to adequately assess source properties of the induced earthquakes, and to also provide realistic estimates of potential shaking levels for future (induced) earthquakes.

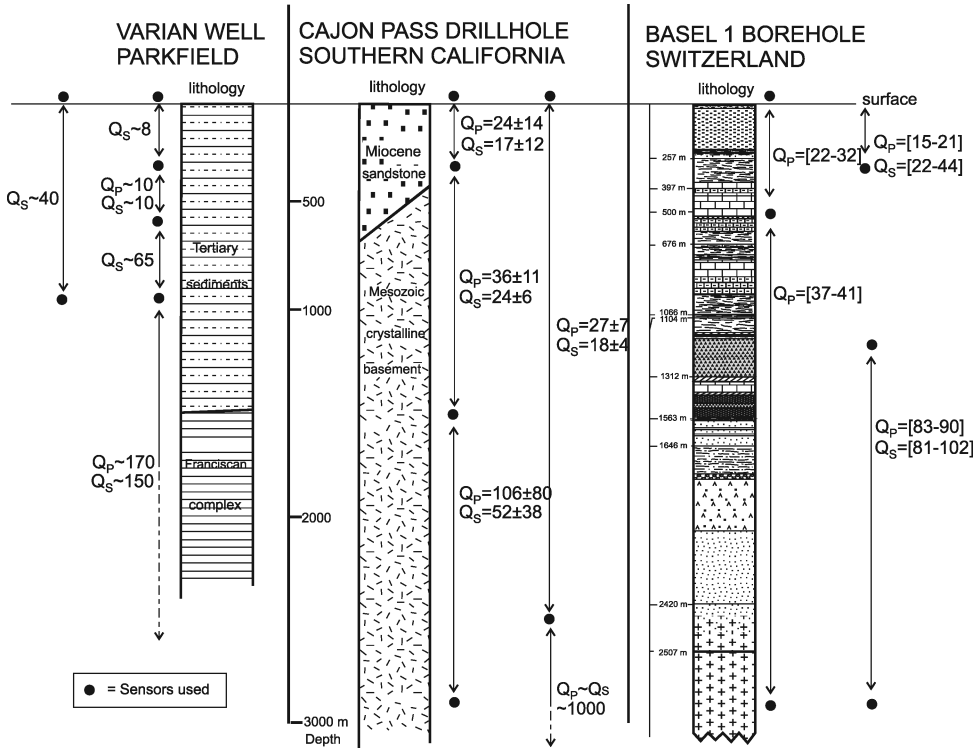

Figure 13. Comparison of attenuation for different rock type. Varian well data are taken from Jongmans & Malin (1995), Cajon Pass data from Abercrombie (1998). The Q values of Basel are selected from Table 1. All three studies show similar Q values independent of rock type and increasing with depth. Figure taken from Abercrombie (1998) and extended with results from Basel.

8 DATA AND RESOURCES

Surface seismograms used in this study were collected by the Swiss Seismological Service and the Erdbebendienst des Landesamtes für Geologie, Rohstoffe und Bergbau Baden Württemberg and are available upon request. Recordings of the borehole seismometers were provided by Geopower Basel and are proprietary and cannot be released to the public. Plots were generated using Matlab and Corel Draw software.

ACKNOWLEDGMENTS

We thank Geothermal Explorers Limited for the access to their borehole logs and 1000 Hz data as well as instrument specifications. We are grateful to Bettina Allmann, Ben Edwards and Toni Kraft for fruitful discussions that helped to improve the manuscript. We thank Dino Bindi and an anonymous reviewer for their comments in the course of this study. The project was funded by the Swiss National Science Foundation (SNF 200021-112284/1).

REFERENCES

Abercrombie, R.E., 1995. Earthquake source scaling relationships from −1 to 5 M_L using seismograms recorded at 2.5-km depth, *J. geophys. Res.,* **100,** 24015–24036.

Abercrombie, R.E., 1997. Near-surface attenuation and site effects from comparison of surface and deep borehole recordings, *Bull. seism. Soc. Am.,* **87**(3), 731–744.

Abercrombie, R.E., 1998. A summary of attenuation measurements from borehole recordings of earthquakes: the 10Hz transition problem, *Pure appl. Geophys.,* **153,** 475–487.

Aki, K. & Richards, P., 2002. *Quantitative Seismology,* 2nd edn, University Science Books, Sausalito, CA.

Asanuma, H., Kumano, Y., Hotta, A., Schanz, U., Niitsuma, H. & Häring, M., 2007. Analysis of microseismic events from a stimulation at Basel, Switzerland., *GRC Transact.,* **31,** 265–269.

Aster, R. & Shearer, P., 1991. High-frequency borehole seismograms recorded in the San Jacinto fault zone, Southern California: part 2. Attenuation and site effects, *Bull. seism. Soc. Am.,* **81,** 1081–110.

Azimi, S., Kalinin, A., Kalinin, V. & Pivovarov, B., 1968. Impulse and transient characteristics of media with linear and quadratic absorption laws, *Izvestiya, Phys. Solid Earth,* 88–93.

Baer, M. *et al.*, 2007. Earthquakes in Switzerland and surrounding regions during 2006, *Swiss J. Geosci.,* **100**(3), 517–528.

Becker, A., 2000. The Jura mountains—an active foreland fold-and-thrust belt?, *Tectonophysics,* **321,** 381–406.

Becker, A., Blümling, P. & Müller, W.H., 1987. Recent stress field and neotectonics in the Eastern Jura Mountains, Switzerland, *Tectonophysics,* **135,** 277–288.

Bronez, T., 1992. On the performance advantage of multitaper spectral analysis, *IEEE Trans. Sig. Proc.,* **12**(40), 2941–2946.

Choy, G. & Boatwright, J., 1995. Global patterns of radiated seismic energy and apparent stress, *J. geophys. Res.,* **100,** 18 205–18 228.

Deichmann, N., 1997. Far-field pulse shapes from circular sources with variable rupture velocities, *Bull. seism. Soc. Am.,* **87**(5), 1288–1296.

Deichmann, N. & Ernst, J., 2009. Earthquakes focal mechanisms of the induced seismicity in 2006 and 2007 below Basel (Switzerland), *Swiss J. Geosci.,* **102**(3), 457–466.

Deichmann, N. & Giardini, D., 2009. Earthquakes induced by the stimulation of an enhanced geothermal system below Basel (Switzerland), *Seism. Res. Lett.,* **80**(5), 784–798.

Dyer, B., Schanz, U., Ladner, F., Häring, M. & Spillmann, T., 2008. Microseismic imaging of a geothermal reservoir stimulation, *Leading Edge,* **27,** 856–869.

Dyer, B., Schanz, U., Spillmann, T., Ladner, F. & Häring, M., 2010. Application of microseismic multiplet analysis to the Basel geotheral reservoir stimulation events, *Geophys. Prospect.,* **58,** 791–807.

Edwards, B., Fäh, D. & Giardini, D., 2011. Attenuation of seismic shear-wave energy in Switzerland, *Geophys. J. Int.,* **185,** 967–984.

Esmersoy, C., 1984. Polarization analysis, orientation and velocity estimation in three component VSP, in *Vertical Seismic Profiling—Part B: Advanced Concepts,* ed. Toksöz, M.N. and Stewart, R. R., Geophysical Press, Benahavis, Spain.

Evans, K. & Roth, P., 1998. *The State of Stress in Northern Switzerland Inferred from Earthquake Seismological Data and in situ Stress Measurements.,* Proseis AG, Sewardstrasse 7, CH-8050, Zürich, Switzerland.

Fäh, D. & Huggenberger, P., 2006. INTERREG III Erdbebenmikrozonierung im südlichen Oberrhein, Zusammenfassung für das Projektgebiet in der Schweiz, CD and report (in German) available from the authors, Swiss Seismological Service, ETH Zurich and Kantonsgeologie, University of Basel.

Fäh, D. *et al.*, 2009. The 1356 Basel earthquake: an interdisciplinary revision, *Geophys. J. Int.,* **178,** 351–374.

Feustel, A.J., Trifu, C. & Urbanicic, T.I., 1996. Rock-mass charcterization using intrinsic and scattering attenuation estimates at frequencies from 400 to 1600hz, *Pure appl. Geophys.,* **147**(2), 298–304.

Gebrande, H., 1976. A seismic ray-tracing method for two-dimensional inhomogenous media, in *Explosion Seismology in Central Europe,* pp. 162–167, eds Glese, P., Prodehl, C., Stein, A., Springer, Berlin.

Gürler, B., Hauber, L. & Schwandner, M., 1987. Die Geologie der Umgebung von Basel mit Hinweisen über die Nutzungsmöglichkeiten der Erdwärme, Tech. Rep. 160, Schweizerische Geologische Kommision, Bern.

Häring, M.O., Schanz, U., Ladner, F. & Dyer, B., 2008. Characterisation of the Basel 1 enhanced geothermal system, *J. Geothermics,* **37,** 469–495.

Hauksson, E., Teng, T.L. & Henyey, T.L., 1987. Results from a 1500m deep, three-level downhole seismometer array: site response, low Q values, and f_{max}, *Bull. seism. Soc. Am.,* **77**(6), 1883–1904.

Hoshiba, M., 1993. Separation of scattering attenuation and intrinsic absorbtion in Japan with the Multiple Lapse Time Window analysis from full seismogram envelope, *J. geophys. Res.,* **98,** 15 809–15 824.

Ide, S. & Beroza, G., 2001. Does apparent stress vary with earthquake size?, *Geophys. Res. Lett.,* **28**(17), 3349–3352.

Jackson, G., Mason, I. & Greenhalgh, S., 1991. Principal component transforms of triaxial recordings by singular value decomposition, *Geophysics,* **56**(4), 528–533.

Jin, A., Mayeda, K., Adams, D. & Aki, K., 1994. Separation of intrinsic and scattering attenuation in southern California using TERRAscope data, *J. geophys. Res,* **99**(B9), 17 835–17 848.

Jongmans, D. & Malin, P.E., 1995. Microearthquake S-wave observations from 0 to 1 km in the Varian Well at Parkfield, California, *Bull. seism. Soc. Am.,* **85**(6), 1805–1820.

Jordan, P., 1994. Evaporite als Abscherhorizonte, eine gefügekundlich-struktur-geologische Untersuchung am Beispiel der Nordschweiz Trias, Beiträge zur geologischenn Karte der Schweiz 164, 79pp.

Kanamori, H.J., Mori Hauksson, E., Heaton, T.H. & Hutton, L.K., 1993. Determination of earthquake energy release and M_L using Terrascope, *Bull. seism. Soc. Am.,* **83**(2), 330–346.

Kind, F., 2002. Developement of microzonation methods: application to Basel, Switzerland, *PhD thesis*, ETH Zürich, Institute of Geophysics.

Kinoshita, S., 2008. Deep-borehole-measured Q_P and Q_S attenuation for two Kanto sediment layer sites, *Bull. seism. Soc. Am.,* **98**(1), 463–468.

Kumano, Y., Asanuma, H., Hotta, A., Niitsuma, H., Schanz, U. & Häring, M., 2007. Reservoir structure delineation by microseismic multiplet analysis at Basel, Switzerland, 2006, *SEG Exp. Abstr.,* **26,** 1271–1276, doi:10.1190/1.272735.

Mayeda, K., Gök, R., Walter, W. & Hofstetter, A., 2005. Evidence for non-constant energy/moment scaling from coda derived source spectra, *Geophys. Res. Lett.,* **32,** L10306, doi:10.1029/2005GL022405.

Opršal, I., Fäh, D., Mai, P. & Giardini, D., 2005. Deterministic earthquake scenario for the Basel area: Simulating strong motions and site effects for Basel, Switzerland, *J. geophys. Res.,* **110,** doi:10.1029/2004JB003188.

Park, J., Lindberg, C. & Vernon, F., 1987. Multitaper spectral analysis of high-frequency seismograms, *J. geophys. Res.,* **92,** 12 675–12 648.

Prejean, S. & Ellsworth, W., 2001. Observations of earthquake source parameters at 2km depth in the Long Valley Caldera, Eastern California, *Bull. seism. Soc. Am.,* **91**(2), 165–177.

Prieto, G.A., Shearer, P., Vernon, F. & Kilb, D., 2004. Earthquake source scaling and self-similarity estimation from stacking P and s spectra, *J. geophys. Res.,* **109,** 1269–1281.

Prieto, G.A., Parker, R.L., Thomson, D., Vernon, F.L. & Graham, R.L., 2007. Reducing the bias of multitaper spectrum estimates, *Geophys. J. Int.,* **171**(3), 1269–1281.

Riedel, K. & Sidorenko, A., 1993. Minimum bias multiple taper spectral estimation, *IEEE Trans. Sig. Proc.,* **43,** 188–195.

Ripperger, J., Kästli, P., Fäh, D. & Giardini, D., 2009. Ground motion and macroseismic intensities of a seismic event related to geothermal reservoir stimulation below the city of Basel—observations and modelling, *Geophys. J. Int.,* **3**(179), 1757–1771.

Rózsa, S., Heck, B., Mayer, M., Seitz, K., Westerhaus, M. & Zippelt, K., 2005. Determination of displacements in the upper Rhine Graben area from GPS and leveling data, *Int. J. Earth Sci. (Geol. Rundsch.),* **94,** 538–549.

Sato, T., 1994. Seismic radiation from circular cracks growing at variable rupture velocity, *Bull. seism. Soc. Am.,* **84,** 1199–1215.

Shearer, P. & Orcutt, J., 1987. Surface and near-surface effects on seismic waves—theory and borehole seismometer results, *Bull. seism. Soc. Am.,* **79,** 1168–1196.

Singh, S.K. & Ordaz, M., 1994. Seismic enery release in mexican subduction zone earthquakes, *Bull. seism. Soc. Am.,* **84,** 1533–1550.

Sommaruga, A., 1999. Décollement tectonics in the Jura foreland fold-and-thrust belt, *Mar. Petrol. Geol.,* **16,** 111–134.

Spottke, I., Zechner, E. & Huggenberger, P., 2005. The southeastern border of the upper rhine graben: a 3d geological model and its impotance for tectonics and groundwater flow, *Int. J. Earth Sci. (Geol. Rundsch),* **94,** 580–593.

Thomson, D.J., 1982. Spectrum estimation and harmonic analysis, *Proc. IEEE,* **70,** 1055–1096.

Ustaszewski, K. & Schmid, S.M., 2007. Latest Pliocene to recent thick-skinned tectonics at the Upper Rhine Graben-Jura Mountains junction, *Swiss J. Geosci.,* **100,** 293–312.

Valley, B. & Evans, K.F., 2009. Stress orientation to 5 km depth in the basement below Basel (Switzerland) from borehole failure analysis, *Swiss J. Geosci.,* **102,** 467–480.

Wu, R., 1985. Multiple scattering and energy transfer of seismic waves—separation of scattering effect from intrinsic attenuation, I, theoretical modeling, *Geophys. J. R. astr. Soc.,* **82,** 57–80.